Divergent allosteric control of IRE1α endoribonuclease using small molecule kinase inhibitors

Arinjay Kumar Mitra

A thesis submitted in partial fulfillment of the

requirements for the degree of

Master of Science

University of Washington

2014

Committee:

Dustin J. Maly

Champak Chatterjee

Program Authorized to Offer Degree:

Chemistry

University of Washington

Abstract

Divergent allosteric control of IRE1α endoribonuclease

using small molecule kinase inhibitors

Arinjay Kumar Mitra

Chair of the Supervisory Committee:

Dustin J. Maly, Associate Professor

Department of Chemistry

When unfolded proteins get accumulated in the endoplasmic reticulum (ER), signaling pathways called the unfolded protein response (UPR) get turned on in the cell. However under conditions of chronic ER stress, the cell undergoes apoptosis. Key events of this "Terminal UPR" are controlled by IRE1α – an ER bifunctional kinase/endoribonuclease (RNase), which when hyperactivated, oligomerizes causing widespread endonucleolytic decay of ER-localized mRNAs and repressive micro-RNA precursors triggering cell death. Somatic mutations of IRE1α found in human cancers prevent oligomerization and inhibit apoptosis caused by the RNase. Using these results, our lab developed an array of ATP-competitive kinase inhibitors – called KIRAs (*K*inase *I*nhibiting *R*Nase *A*ttenuators) – that inhibit oligomerization of the IRE1α kinase domain and allosterically inhibit the RNase. In this work we have made efforts to expand the existing panel of KIRAs, looking to achieve greater potency and selectivity towards IRE1α and understand IRE1α mechanism of action.

Introduction

Almost a third of the eukaryotic proteome is either inserted into membranes, secreted to exteriors of the cell exterior, or transported to intracellular organelles. These proteins of the secretory pathway first pass through the endoplasmic reticulum (ER) as they fold and structurally mature. ER-localized chaperones, glycosylating enzymes, and oxido-reductases usually catalyze these processes[1]. The ER in said to be under "stress" when the workload on these ER protein-folding and modification functions exceeds capacity. ER stress can be a product of elevated rates of protein secretion, high expression of folding-defective secretory proteins, and lack of oxygen and nutrients. Such deviations from normalcy activate intracellular signaling pathways termed the unfolded protein response (UPR) that increase transcription of genes encoding chaperones, ER-associated degradation (ERAD) components, and oxidoreductases[2]. The UPR also stalls translation albeit temporarily to reduce the load of unfolded proteins in the ER[3]. These are adaptive measures because they enhance the capacity for protein-folding and promote degradation of unfolded proteins[4,5,6], consequently restoring ER homeostasis.

However, in the event of chronic/irremediable ER stress, the UPR shifts from the adaptive pathway, relegating cells to apoptosis through destructive outcomes called the "Terminal UPR." Although this might seem deleterious, apoptosis induced by the Terminal UPR may protect multicellular organisms from exposure to nascent, misfolded secretory proteins. Conversely, uncontrolled cell degeneration under ER stress have been implicated, at least partially, in many human diseases such as diabetes mellitus, retinopathies, multiple myeloma and a host of other neurodegenerative disorders[7,8,9]. Therefore, elucidating underlying mechanisms of the Terminal UPR may lead to effective therapies for such conditions.

Intracellular signals transmitted by the UPR are integrated by cells to make one of two decisions: either allow the cells to survive under remedial stress, or relegate them to apoptosis in the event that homeostasis cannot be restored. Three ER transmembrane sensors, PERK, ATF6, and IRE1α, get activated by accumulation of unfolded ER proteins, which in turn, undergo changes in their oligomerization state. The most ancient of these signaling proteins, IRE1α, senses unfolded proteins, directly or indirectly, through an ER lumenal domain which oligomerizes during stress[10,11]. As a result of oligomerization, IRE1α's Serine (Ser)/Threonine (Thr) kinase domains get juxtaposed onto each other, which consequently *trans*-autophosphorylate. The adjacent RNase domain gets activated due to kinase autophosphorylation, cleaving XBP1 mRNA site-specifically to excise a 26-nucelotide intron. Translation of spliced XBP1 mRNA generates the transcription factor XBP1s (s=spliced)[12,13]. XBP1s gene targets encode chaperones that enhance ER protein folding[14]. Therefore, IRE1α allows the cell to adapt to ER stress via XBP1s.

Lower levels of IRE1α auto-phosphorylation caused by remediable ER stress limits its RNase activity to XBP1 mRNA splicing. Irremediable ER stress, on the other hand, hyperactivates IRE1α promoting sustained kinase autophosphorylation, resulting in the endonucleolytic decay of thousands of ER-localized mRNAs and precursor forms of microRNAs that inhibit apoptosis[15,16,17], causing programmed cell-death. Although activation of IRE1α's RNase is normally dependent on kinase autophosphorylation[18], we identified an unusual relationship between the kinase and RNase domains that allows ligands of the kinase domain to bypass the autophosphorylation requirement and trigger RNase activation allosterically[19]. For instance, the orthogonal ATP-competitive inhibitor 1NM-PP1 rescues RNase activity of IRE1α mutants that lack kinase activity[15,19]. Other ligands that bind to the ATP-binding site of wild-type (WT) IREα also activate the RNase. For example, the promiscuous type I ATP-competitive inhibitor APY29

and the clinically-approved drug sunitinib activate the yeast RNase[20] and murine IRE1α[15]. A crystal structure of APY29 bound to yeast IRE1 shows that the kinase catalytic domain is in an *active* conformation (**Figure 1a**).

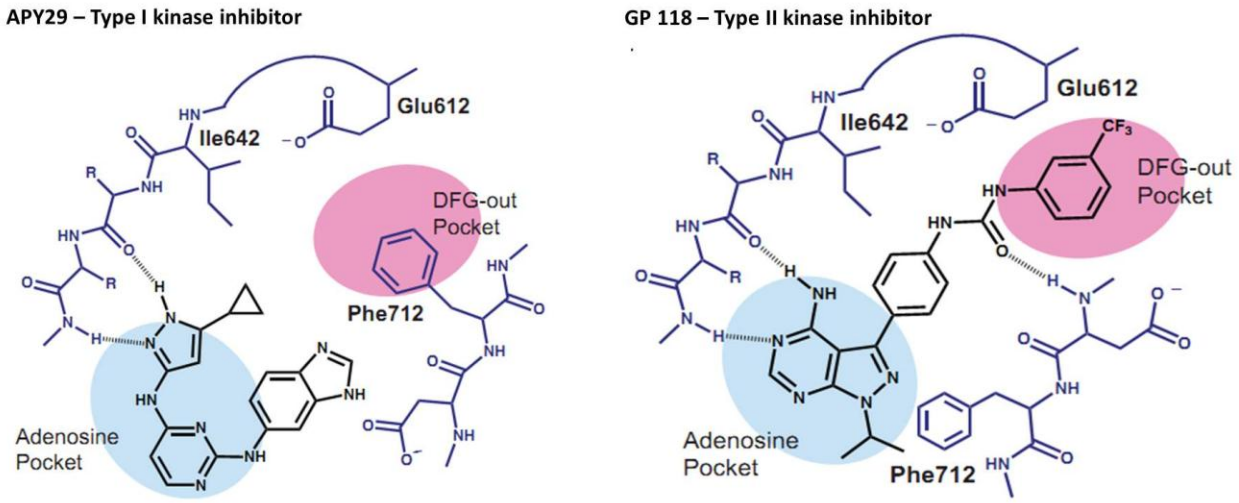

Fig 1: a) Type 1 inhibitor APY29 bound to yeast IRE1α. **b)** Proposed contacts of Type II inhibitor GP 118 with IRE1 based on co-crystal structure of GP118 bound to Src.

Given the ability to allosterically *activate* IRE1α's RNase through the kinase domain, we hypothesized that it may be possible to *inhibit* the RNase through the same domain (**Figure 2**). In a previous study, we showed that compounds stabilizing an *inactive* kinase active site conformation would disable IRE1α's RNase allosterically. Several small molecule inhibitors selective for *inactive* forms of the ATP-binding site of protein kinases— the Asp-Phe-Gly (DFG)-out, α-C helix out—have been described, including the clinically-approved drugs imatinib and sorafenib[29]. This class of ligands, called type II inhibitors, stabilize an inactive ATP-binding site conformation characterized by the outward movement of the catalytically-important DFG-motif/α-C helix [21,22]. These results suggest that through selective targeting of

IRE1α's kinase domain, its RNase activity can be either up- or down-regulated, thus affecting cell-fate in both positive (pro-survival) and negative (pro-apoptotic) directions.

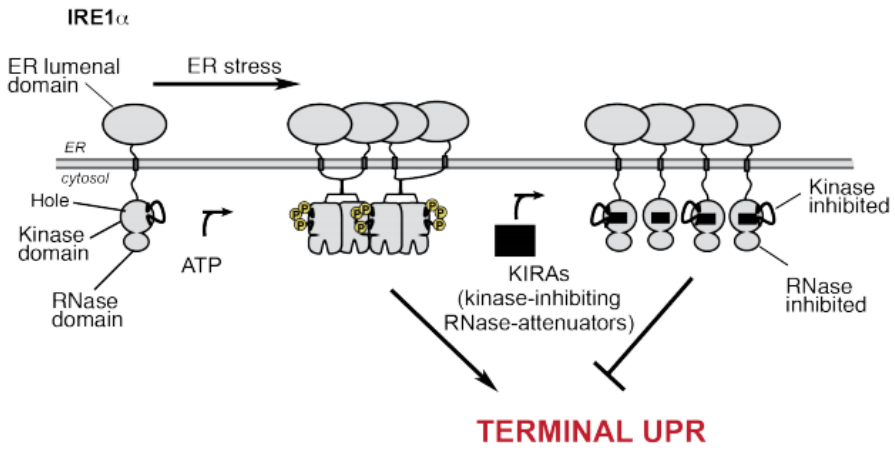

Fig 2: Proposed model for allosteric inhibition of IRE1α RNase using Type II kinase inhibitors (KIRAs).

Functionalization of Type II kinase inhibitors

In order to achieve greater potency and selectivity towards IRE1α and gain insight into the binding mode of these inhibitors, we considered introducing a range of structural modifications keeping certain core elements constant. In a previous study, GP 146 (KIRA3) was shown to be the most potent in a series of type II kinase inhibitors tested against IRE1α[23]. It was also shown to be relatively non-toxic to cells. Therefore, KIRA3 seemed to be a promising starting point.

Based on the co-crystal structure of Type II inhibitor GP118 (KIRA1) bound to non-receptor tyrosine kinase Src, molecular docking analysis was performed to yield probable favourable contacts that the inhibitor might make with the ATP-binding pocket of IRE1α (**Fig 1b**). Keeping these binding interactions in mind, we wanted to modify KIRA3 to potentially include a Michael-acceptor group in the DFG-out pocket, the rationale being that it might allow the

formation of a covalent linkage with an active site cysteine residue thus enhancing potency against IRE1α kinase inhibiton. However, a recent co-crystal structure of KIRA3 bound to Src kinase domain (**Figure 3**) suggests that KIRA3 stabilizes another inactive conformation of Src called the alpha-C helix out conformation which arises due to the outward movement of the alpha-C helix of its kinase domain. Since IRE1α could potentially also adopt this conformation, there is a possibility that these type II imidazo-pyrazine based inhibitors inhibit IRE1α by stabilizing its alpha C-helix out conformation as opposed to the previously considered DFG-out conformation. In that case, the active site cysteine residue would not be accessible to the ligand. Also, in crystal structures of inactive IRE1α, the helix αC is flipped out. In addition, this shift in the helix alpha-C disrupts the dimer interface, destabilizing higher order oligomers and might prove to be the mechanism by which KIRAs reduce oligomerization of the IRE1α kinase domains. Hence, we steered away from introducing a Michael-acceptor group in the hydrophobic pocket. However, we are still not certain as to which inactive conformation is stabilized by KIRAs, since we are yet to obtain a co-crystal structure of any of our inhibitors bound to IRE1α.

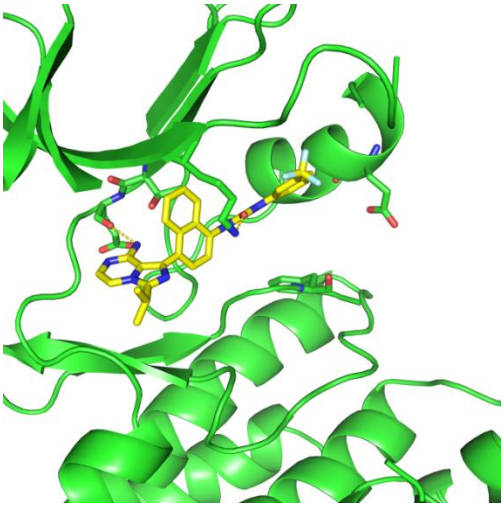

Fig 3: KIRA3 binds to Src in the alpha C-helix out conformation.

While efforts were being made to understand the binding mode of Type II inhibitors using crystallography, we decided to make specific modifications in the KIRA molecular skeleton to gain insight into possible binding interactions in the ATP-binding site. The changes we wanted to introduce were primarily focused on four sections of the core scaffold: alkyl/aryl groups coming off the imidazo-pyrazine ring in the adenine pocket, the DFG-out/ αC helix-out pocket, the intervening region between the two, and the urea-linkage connecting them. So far we have successfully synthesized analogs AM001 through AM030, including AM018 (control compound which disrupts one of the hydrogen bonds in the hinge region of the ATP-binding pocket) (**Figure 4**).

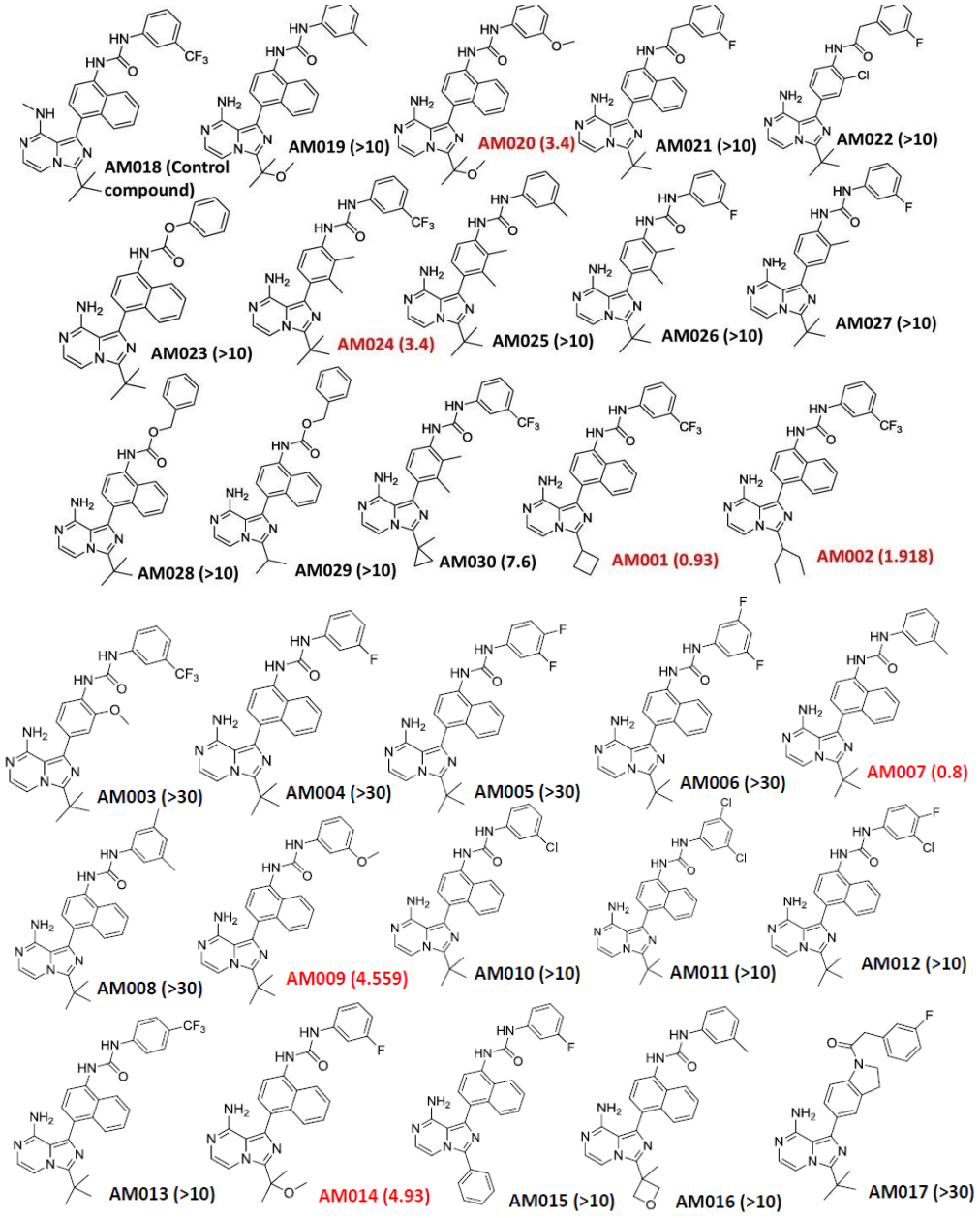

Fig4: List of synthesized compounds and their kinase IC_{50}s against IRE1α (μM). The compounds showing inhibition against IRE1α have been highlighted in red.

We adopted a synthesis approach that involved making a core imidazo-pyrazine scaffold starting from an amino chloro-pyrazine, which was consequently coupled to various boronic ester

ureas/methylene amides/carbamates depending on the kind of linker we wanted to introduce in our analogs (**Figure 5**).

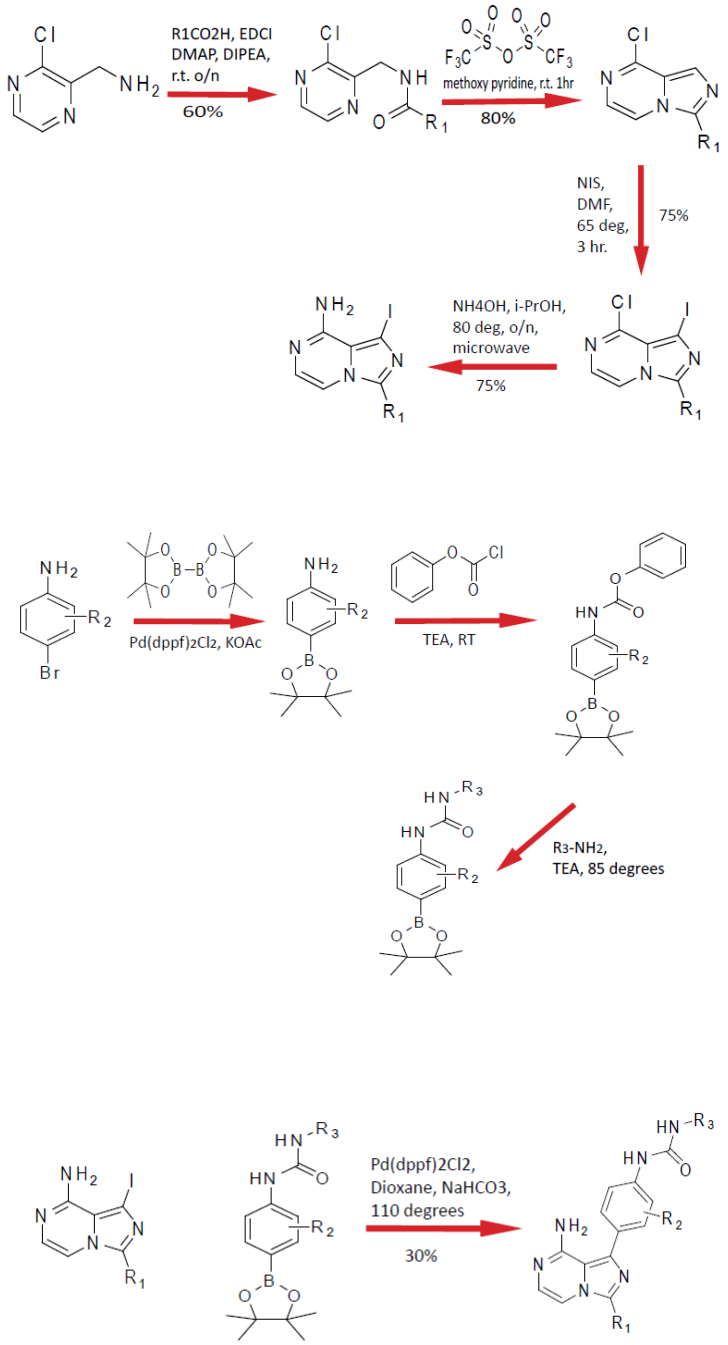

Fig 5. Synthetic protocol for generating imidazo-pyrazine based inhibitors.

Determining potency of Type II kinase inhibitors (KIRAs) against IRE1α kinase

In order to determine the efficacy of KIRAs towards IRE1α kinase inhibition, we carry out an activity assay using γ-^{32}P labelled ATP. The lower the half-maximal inhibitory concentration values (IC_{50}), the more potent is the corresponding kinase inhibitor. Towards this effect, we initially tested some of the newly-synthesized inhibitors against IRE1α along with some previously synthesized imidazo-pyrazine analogs KIRA3, GP165, GP166, GP167, GP159, GP162, GP163, GP157, GP150, GP151 (**Figure 6**) and pyrazole-pyrimidine analogs GP106, GP120, GP127, GP118, GP 154, GP121, GP122, SL1, SL2 (**Figure 7**) against IRE1α.

The IC_{50} values for the imidazo-pyrazine inhibitors in general were found to be lower (mostly nanomolar) than the pyrazole-pyrimidine inhibitors (micromolar). From the observed IC_{50}s, it was apparent that the imidazo-pyrazine scaffold contributed towards potency. Therefore, we decided to derivatize other parts of the molecular skeleton, retaining the imidazo-pyrazine core.

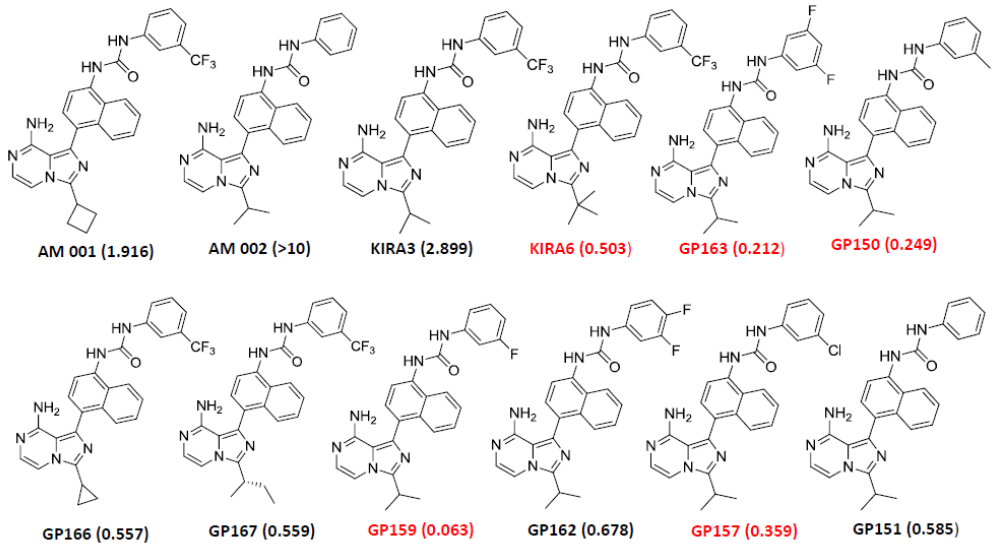

Fig 6: Imidazo-pyrazine based inhibitors initially tested against IRE1α. The numbers in parenthesis are the kinase IC50s (micromolar).

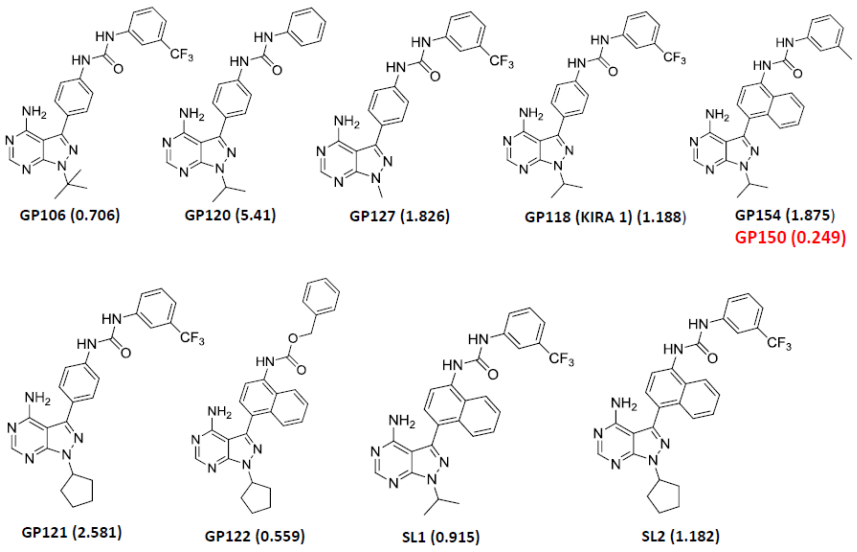

Fig 7: Pyrazole-pyrimidine based inhibitors initially tested against IRE1α. The numbers in parenthesis are the kinase IC50s (micromolar).

Determining potency of Type II kinase inhibitors (KIRAs) against IRE1α RNase

To determine the effect of kinase inhibitors on RNase activity, we use a Fluorescence Resonance Energy Transfer (FRET) assay, which involves an XBP1 mini-substrate containing a 5'-Carboxyfluorescein and a 3'-Black Hole Quencher (BHQ). This RNA substrate contains the site where IRE1α specifically cleaves XBP1 mRNA in cells, as a part of the adaptive branch of the UPR. Since IRE1α is basally autophosphorylated, the RNase is autoactive. An active RNase cleaves the substrate site-specifically, leading to FRET dequenching. Therefore, a decrease in fluorescence signal serves as a direct readout of RNase inhibition.

Derivatizing the R group hanging off the imidazo-pyrazine ring while retaining all other structural elements of KIRA3, we noticed that replacing the isopropyl moiety (as in KIRA3) with t-butyl or cyclopropyl methyl groups knocked back both kinase IC50 and RNase EC50 by about

10-fold. The cyclopropyl methyl derivative PR100 turned out to be the most effective IRE1α kinase/RNase inhibitor in the group. (**Figure 8**)

Keeping the cyclopropyl methyl attached to the imidazo-pyrazine core, we focused on functionalizing the intervening naphthyl region. Because naphthyl rings are metabolic liabilities and add to the molecular weight of the inhibitors, we made efforts to replace it with smaller phenyl/substituted phenyl rings. Unfortunately, all the modifications that we did try to introduce seemed to knockback kinase/RNase inhibition significantly. This meant that the naphthyl ring, at least with respect to other elements of this particular scaffold, was critical for inhibition. It most likely made favorable hydrophobic/stacking interactions with other residues in the kinase ATP-binding site. (**Figure 8**)

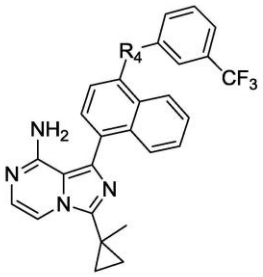

R4	Kinase IC50 (uM)	RNase EC50 (uM)
PR100 	0.14	0.091
HF1105 	18	15
HF1107 	6.6	6.0

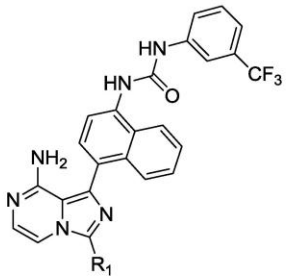

R1	Kinase IC50 (uM)	RNase EC50 (uM)
PR100 	0.14	0.091
KIRA6 	0.165	0.124
GP166 	0.262	0.477
KIRA3 	1.256	1.8
AM001 	0.93	0.175
PR120 	0.678	0.33

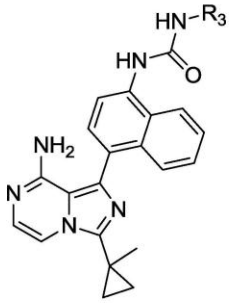

R3	Kinase IC50 (uM)	RNase EC50 (uM)
PR100 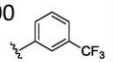	0.14	0.091
PR123 	0.428	0.186
PR135 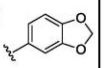	0.89	0.175
HF26 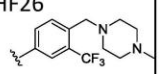	0.843	0.186
HF24 	2.0	6.0

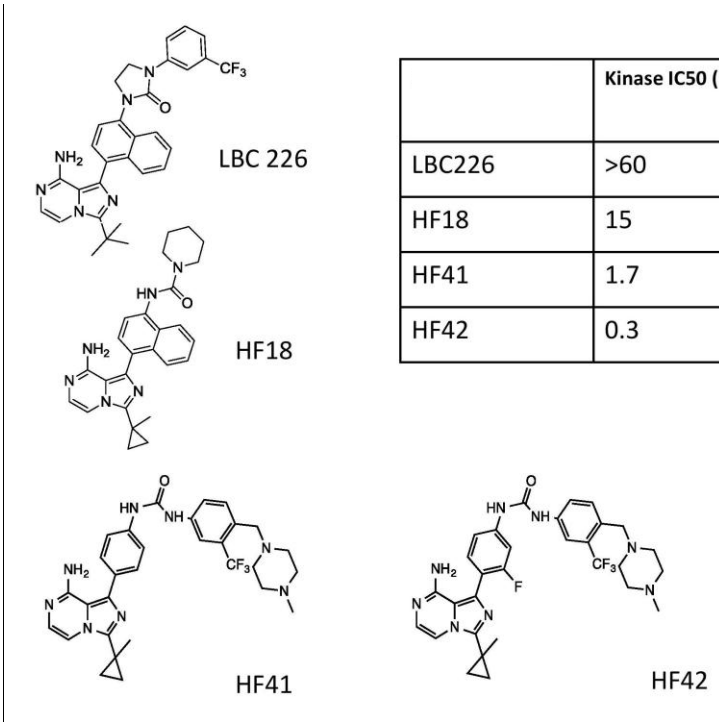

	Kinase IC50 (uM)	RNase EC50 (uM)
LBC226	>60	>60
HF18	15	20
HF41	1.7	1.3
HF42	0.3	0.6

Fig 8: Modifications made to KIRA scaffold to explore binding interactions in the kinase active site.

Among the modifications made in the hydrophobic pocket afforded by outward movement of the DFG motif/helix αC, the 3-trifluoromethyl phenyl group proved to be the most effective. The urea linkage also seemed to be important for inhibition. One of the urea NH groups possibly made favorable hydrogen bonding interactions as is evident from the complete lack of inhibition in LBC226. Inhibitors like HF42 that combine modifications in more than one region of the scaffold, held promise from a potency standpoint. (**Figure 8**)

Over a hundred compounds have been screened against IRE1α kinase and RNase till date. Almost seventy of them showed dose dependent inhibition. However, only ten of these analogs have IC_{50}s lower than 0.5 μM (**Figure 9**). Interestingly, all the compounds tested afford complete inhibition of both IRE1α kinase and RNase at sufficiently high concentrations. In addition, there

is excellent correlation between kinase IC50s and RNase EC50s across the board, reaffirming the causative relationship between kinase domain oligomerization and RNase activation.

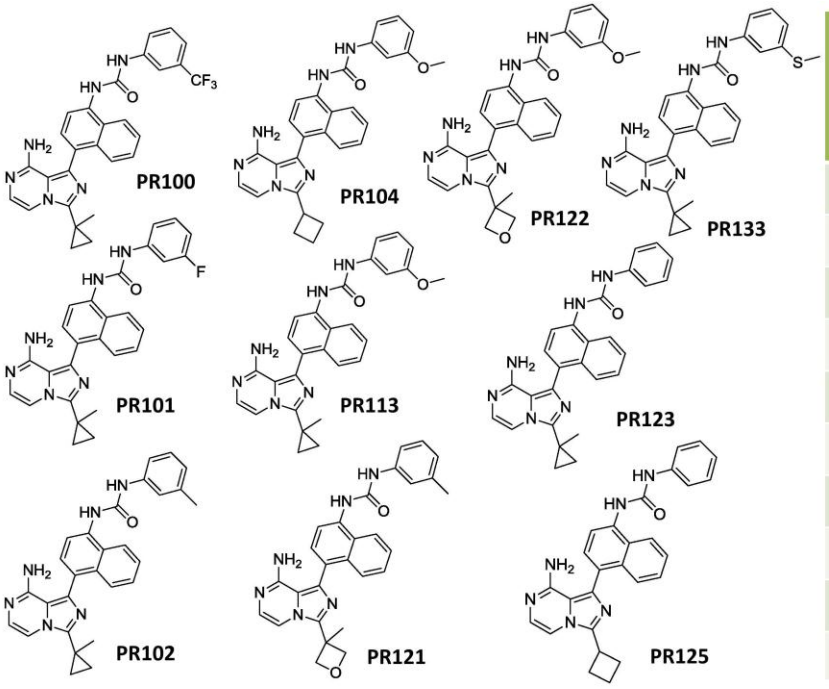

Cmpd ID	Kinase IC50 (uM)	RNase EC50 (uM)
PR100	0.14	0.091
PR101	0.107	0.051
PR102	0.268	0.26
PR104	0.226	0.209
PR113	0.332	0.312
PR121	0.484	0.270
PR122	0.422	0.023
PR123	0.428	0.186
PR125	0.495	0.133
PR133	0.32	0.137

Fig 9: Compounds having IC50s lower than 0.5μM against IRE1α kinase. Their corresponding EC50s against IRE1α RNase have also been listed for comparison.

Exploring residues involved in catalytic function of IRE1α

We next wanted to investigate the residues that might be critical for IRE1α enzymatic activity. In order to do that, we expressed two constructs of IRE1α in SF9 insect cells using the Bac-to-bac baculovirus expression system: a longer IRE1α 469-977 (which includes the linker region that connects the catalytic domains to the transmembrane segment, along with the kinase and RNase domains) and a shorter IRE1α 547-977 (containing only the two catalytic domains without the linker region residues). Since the enzymes were expressed in the baculovirus system, both

constructs were basally autophosphorylated. We also generated dephosphorylated versions of the same by incubating with λ-Phosphatase followed by a quench step with Na_3VO_4.

Untreated and dephosphorylated forms of both IRE1α constructs were derivatized using iodoacetamide, digested with trypsin and consequently subjected to MS analysis. The residues that we primarily focused on in our phosphomapping experiments were serines 548,549,551 and 562 in the linker region and serines 724,726,729 in the activation loop. (**Figure 10**)

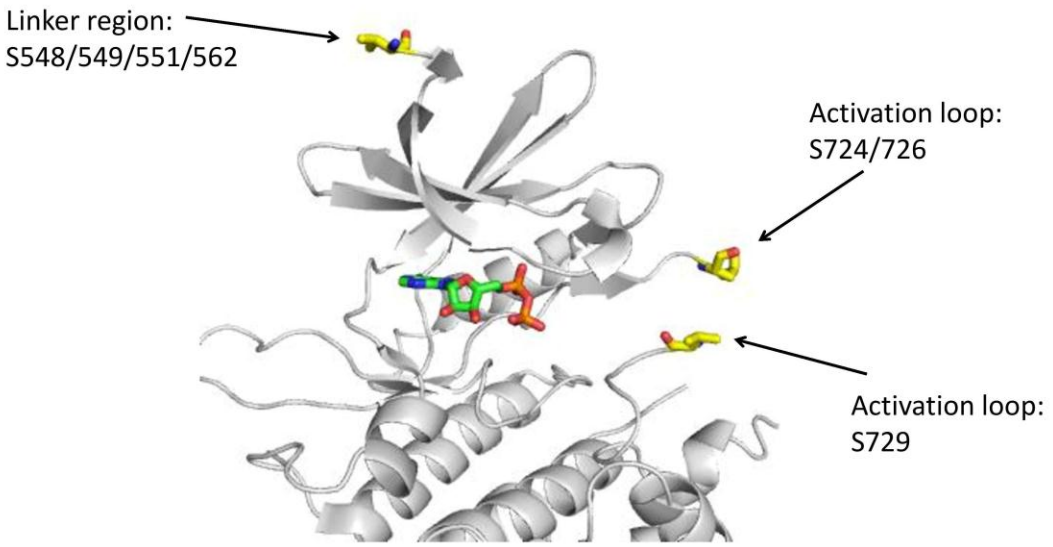

Fig 10: Crystal structure of human IRE1α showing linker region and activation loop residues.

In both constructs, the phosphophorylation state of the linker region serine residues remained unaltered even after incubation with phosphatase, which meant that they were probably not critical for enzymatic activity of IRE1α. In case of IRE1α 469-977, S724/726 went from being 50% diphosphorylated to almost completely unphosphorylated and S729 went from being 50% phosphorylated to almost completely unphosphorylated. Similarly in IRE1α 547-977, S724/726

went from being 80% diphosphorylated to almost completely unphosphorylated. S729 was hardly phosphorylated in the untreated IRE1α 547 construct to begin with. Hence we could not determine any changes in its phosphorylation levels on incubation with phosphatase. However, we could safely conclude that phosphorylation of the activation loop residues seemed to be critical for catalytic function of IRE1α.

We also made efforts to hyperphosphorylate untreated IRE1α and rephosphorylate the enzyme by adding ATP after incubation with phosphatase. For hyperphosphorylation, we incubated untreated IRE1 469 and 547 with 1 mM ATP. In both constructs, we see slight phosphorylation of S729. However, the phosphorylation state of the linker region residues remained unchanged. Increasing ATP incubation time from 1 to 3 hours also did not seem to make any difference. For rephosphorylation, we tried incubation with 1 mM ATP at RT for 3/6 hours and also at 37^0C for 3 hours. Unfortunately, none of these conditions rendered any significant phosphorylation of dephosphorylated residues. Recently we came across a buffer that affords considerably high RNase activity at lower enzyme concentrations in our XBP1 FRET assay. We plan to use this buffer to try and hyperphosphorylate/rephosphoryalate IRE1α in order to gain a better understanding of which residues specifically modulate enzymatic activity.

Effect of type II inhibitors on enzyme behaviour

Now that we had zoomed in on the residues that needed to be phosphorylated for the enzyme to retain its catalytic function, we wanted to investigate how our small molecule Type II inhibitors affected enzymatic behavior at high and low enzyme concentrations. To compare kinase activities, we performed a series of activity assays using radiolabelled ATP where we titrated in the enzyme (IRE1α 469 and 547, untreated and dephosphorylated) ranging from lower

nanomolar to low millimolar concentrations. We performed a similar enzyme titration using the XBP1 FRET assay to compare RNase activities.

a)

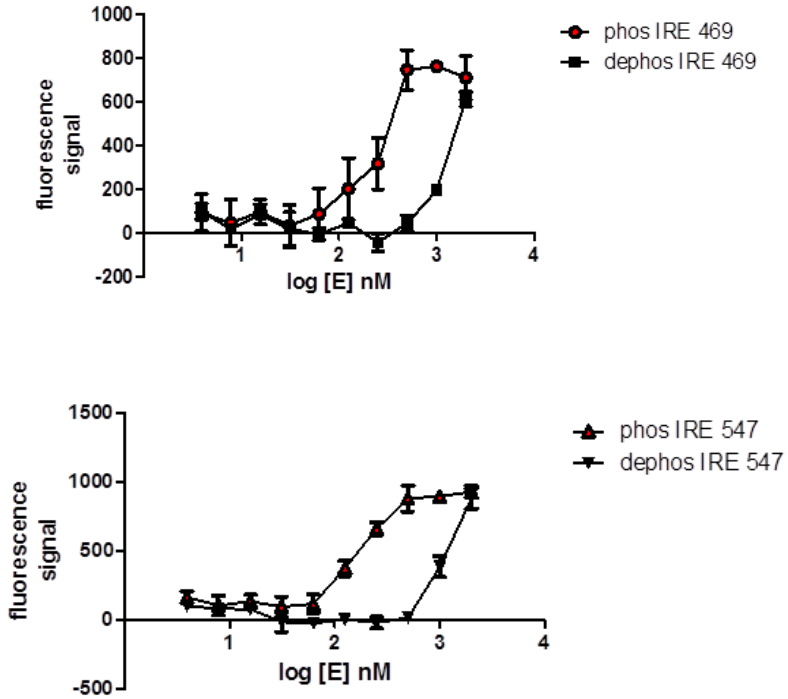

b)

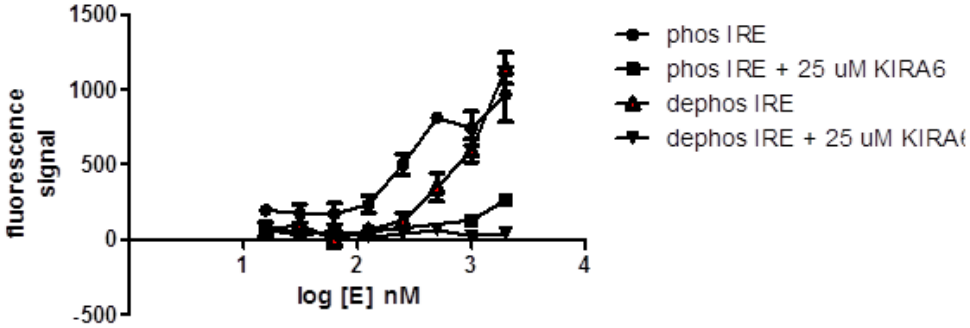

Fig 11: a) RNase activity profile of IRE1α 469 and 547 without type II inhibitor. b) RNase activity profile of IRE1α 469 with KIRA6.

Looking at the plots, we noticed that at higher enzyme concentrations, interestingly, both kinase and RNase activities of dephosphorylated enzyme gradually increase and eventually become comparable to that of their corresponding phosphorylated forms (**Figure 11**). This suggests that even after all basal phosphorylation had been removed, if we go sufficiently high in enzyme concentration, possible formation of higher order oligomers rescues RNase activity and renders the autophosphorylation requirement redundant. To confirm that RNase activation at higher enzyme concentrations was due to oligomerization and not a result of some unknown mechanism, we titrated in untreated and dephosphorylated IRE1α 469 in the presence of Type II inhibitor KIRA6. We observe that in presence of KIRA6, RNase activity of dephosphorylated IRE1α at high enzyme concentrations completely goes away yielding a somewhat "super-dephosphorylated" version of the enzyme (**Figure 11**). Since KIRA6 is known to stabilize IRE1α monomers, it confirms that RNase activation at higher concentrations was due to formation of oligomeric species and that oligomerization was sufficient for an active RNase.

In addition, both untreated and dephosphorylated versions of IRE1α 547-977 were more active than the corresponding versions of IRE1α 469-977. Since basal phosphorylation levels for both constructs were not similar to begin with as revealed by our phosphomapping experiments, we cannot attribute the difference in kinase/RNase activity between the two untreated enzyme contructs to the linker region. However, performing crosslinking experiments with dephosphorylated IRE1α 469 and 547 using disuccinimidyl suberate(DSS) (that crosslinks lysines, and separates oligomeric species on protein gels) can shed some light on the potential role of the linker region in oligomerization and enzymatic function.

Future directions

Signaling pathways that are activated downstream of IRE1α have not yet been characterized fully. We intend on using INS1 cells expressing 3 different forms of IRE1α: WT, and mutants K599A (kinase dead: no autophosphorylation, no oligomerization, no RNase activation) and N906A (RNase dead: kinase autphosphorylation and oligomerization intact, no RNase catalytic activity) for quantitative proteomics (SILAC). Cultured cells in heavy and light media will be incubated with Tg/doxycycline (an antibiotic causing overexpression of IRE1α) for different time points following which cells will be lysed. Lysates will be run on non-specific resin that captures about ~350 proteins. Captured proteins will be digested using trypsin and subjected to MS analysis. This set of experiments should give us some information about what signaling pathways are activated downstream of IRE1α under ER stress/overexpression conditions and what role IRE1α hyperactivation plays on cell signaling in general.

Materials and Methods

Synthesis: The synthetic route shown in Figure 4 was followed in order to generate the panel of imidazo-pyrazine inhibitors. Mass spectrometry (MS) was carried out on a Bruker Esquire Ion Trap MS instrument. The purities of all final compounds were determined by analytical HPLC with two different solvent systems. Analytical conditions A: [C18 (150 x 2.1 mm), CH3CN/H2O-0.1% CF3CO2H = 1:99 to 100:0 over 33 min; 1 mL/min; 220 and 254 nm detection for 33 min]. Analytical conditions B: [C18 (150 x 2.1 mm), CH3OH/H2O-0.1% CF3CO2H = 1:99 to 100:0 over 33 min; 1 mL/min; 220 and 254 nm detection for 33 min]. HPLC traces in both solvent systems along with MS information for our most potent inhibitors PR100, PR101, PR102, PR104, PR113, PR121, PR122, PR123, PR125 and PR133 have been included in the subsequent section.

PR100: The reaction was diluted in acetonitrile/water and purified using General HPLC conditions.

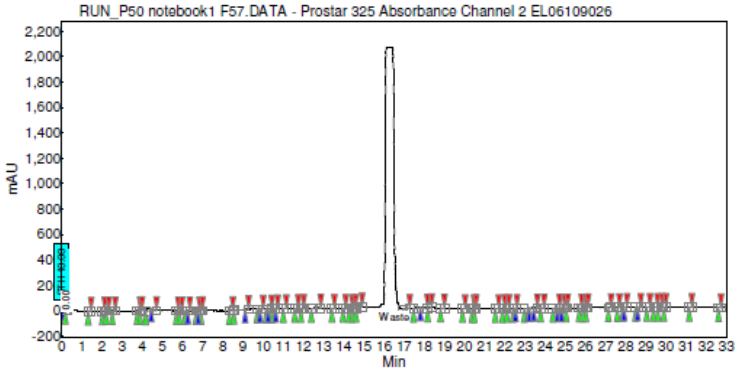

The reaction was diluted in methanol/water and purified using General HPLC conditions.

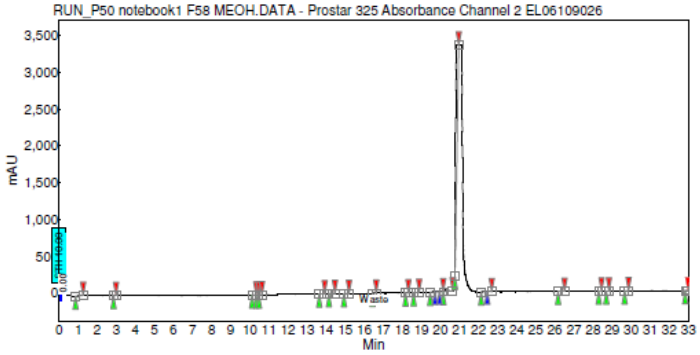

Calculated for $C_{28}H_{23}F_3N_6O$ ($M+H^+$): 516.2; found 517.4.

PR101: The reaction was diluted in acetonitrile/water and purified using General HPLC conditions.

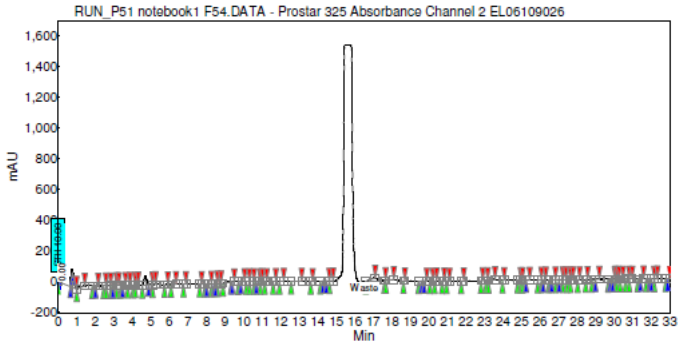

The reaction was diluted in methanol/water and purified using General HPLC conditions.

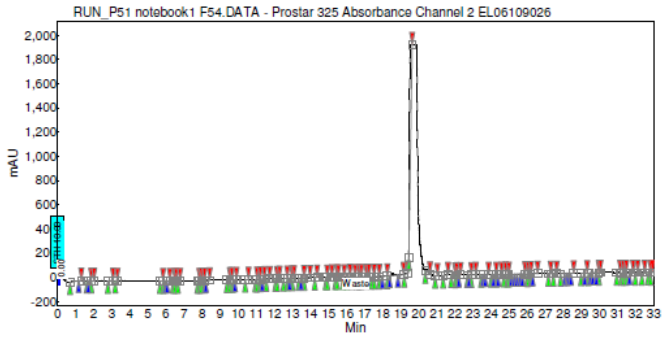

Calculated for $C_{27}H_{23}FN_6O$ ($M+H^+$): 466.2; found 467.6.

PR102: The reaction was diluted in acetonitrile/water and purified using General HPLC conditions.

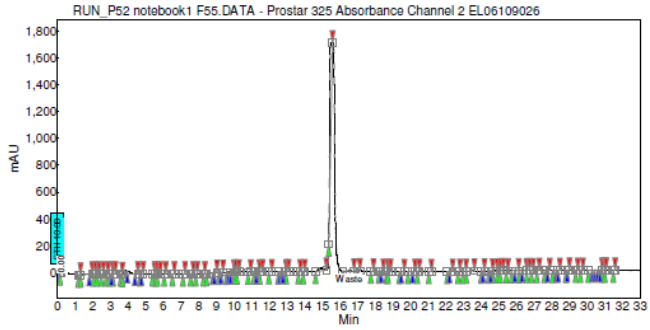

The reaction was diluted in methanol/water and purified using General HPLC conditions.

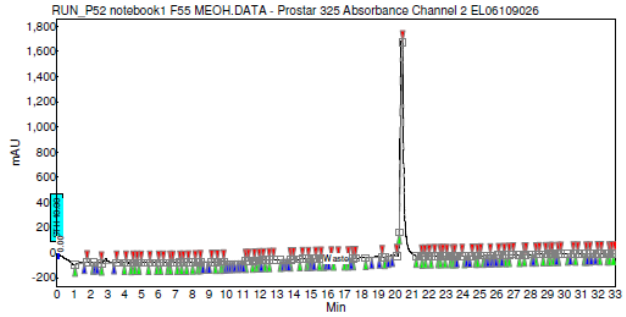

Calculated for $C_{28}H_{26}N_6O$ ($M+H^+$): 462.2; found 463.4.

PR104: The reaction was diluted in acetonitrile/water and purified using General HPLC conditions.

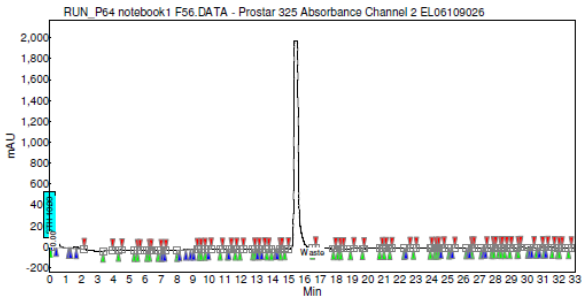

The reaction was diluted in methanol/water and purified using General HPLC conditions.

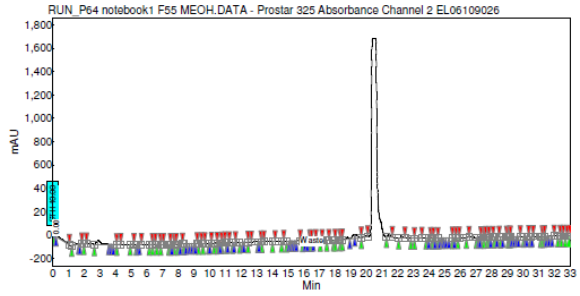

Calculated for $C_{28}H_{26}N_6O_2$ ($M+H^+$): 478.2; found 479.7.

PR113: The reaction was diluted in acetonitrile/water and purified using General HPLC conditions.

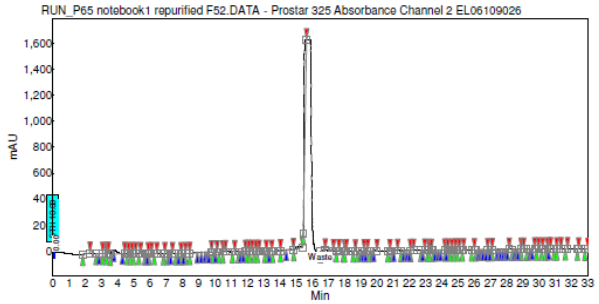

The reaction was diluted in methanol/water and purified using General HPLC conditions.

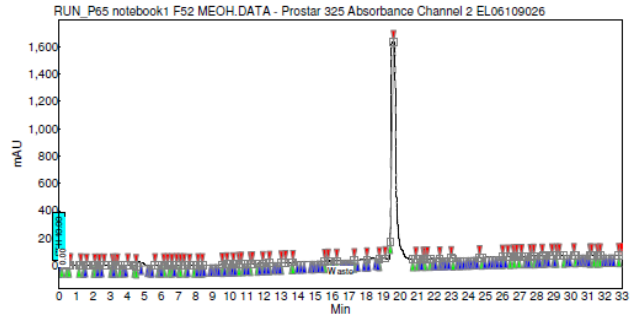

Calculated for $C_{28}H_{26}N_6O_2$ ($M+H^+$): 478.2; found 479.6.

PR121: The reaction was diluted in acetonitrile/water and purified using General HPLC conditions.

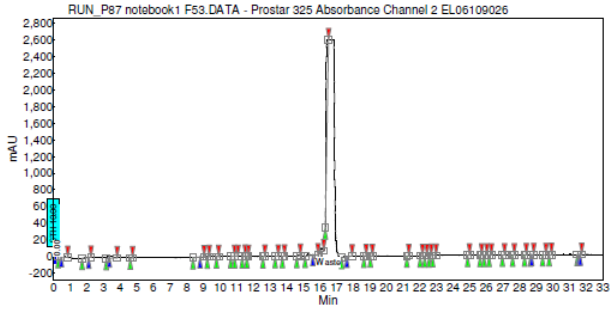

The reaction was diluted in methanol/water and purified using General HPLC conditions.

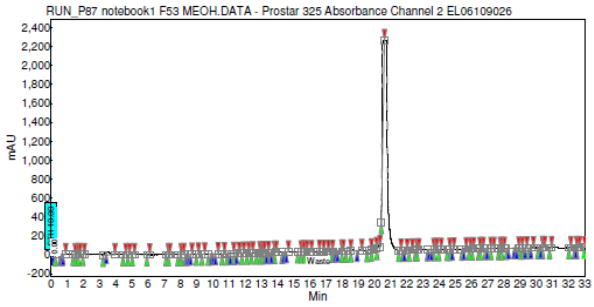

Calculated for $C_{28}H_{26}N_6O_2$ ($M+H^+$):478.2; found 479.4.

PR122: The reaction was diluted in acetonitrile/water and purified using General HPLC conditions.

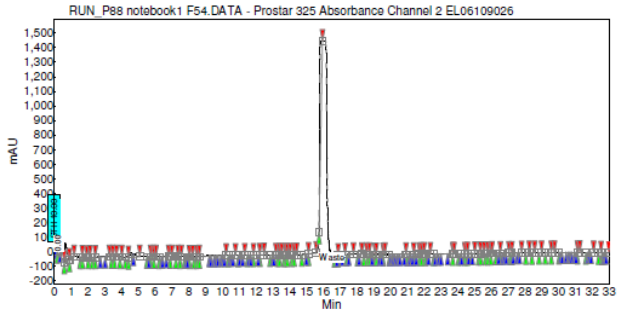

The reaction was diluted in methanol/water and purified using General HPLC conditions.

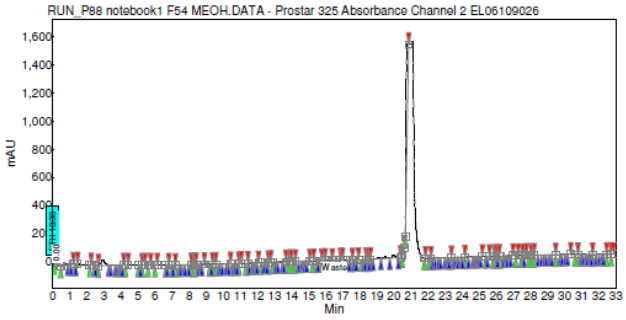

Calculated for $C_{28}H_{26}N_6O_3$ ($M+H^+$): 494.2; found 495.5.

PR123: The reaction was diluted in acetonitrile/water and purified using General HPLC conditions.

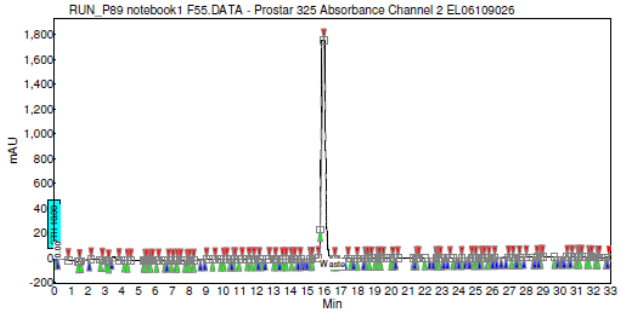

The reaction was diluted in methanol/water and purified using General HPLC conditions.

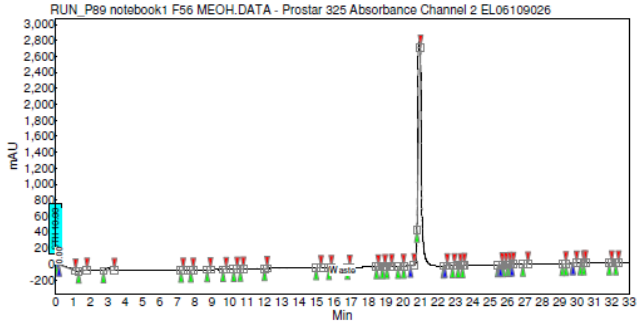

Calculated for $C_{27}H_{24}N_6O$ ($M+H^+$): 448.2; found 449.6.

PR125: The reaction was diluted in acetonitrile/water and purified using General HPLC conditions.

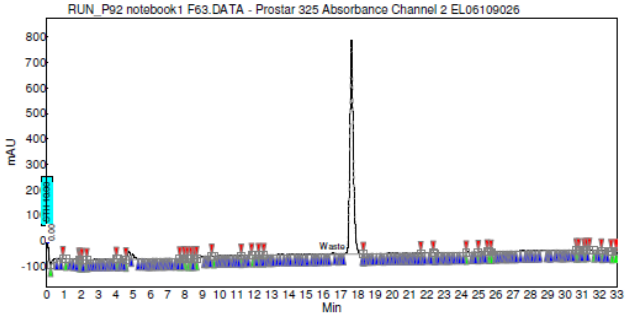

The reaction was diluted in methanol/water and purified using General HPLC conditions.

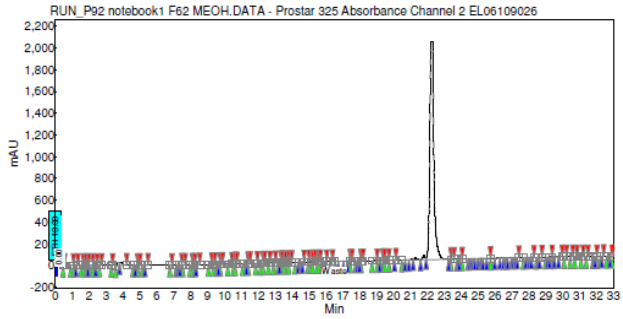

Calculated for $C_{27}H_{24}N_6O$ ($M+H^+$): 448.2; found 449.4.

PR133: The reaction was diluted in acetonitrile/water and purified using General HPLC conditions.

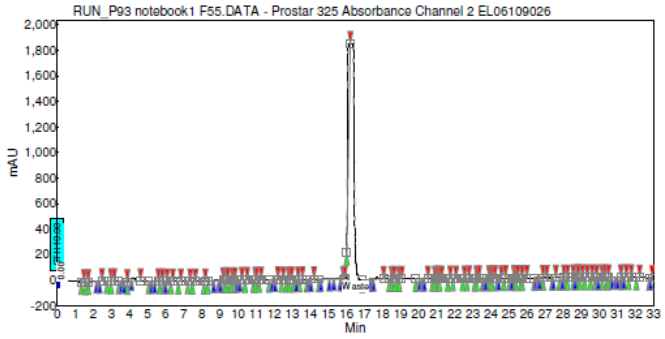

The reaction was diluted in methanol/water and purified using General HPLC conditions.

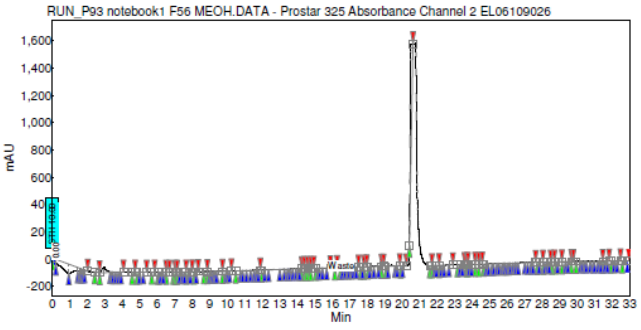

Calculated for $C_{28}H_{26}N_6OS$ ($M+H^+$): 494.2; found 495.5.

In vitro activity assay: Inhibitors (final concentration 10 µM, 3-fold dilutions) were assayed in triplicate against IRE1α, and PERK (final concentration 8.0 nM, and 3.3 nM respectively) in assay buffer containing 50 mM HEPES, pH=7.5, 1 mM MnCl2, 100 mM NaCl, 2 mM DTT, and 0.01% Brij 97 and γ32P ATP (0.2 µCi/well) and Myelin Basic Protein (MBP) (final concentration 0.2 mg/mL). The final volume of each assay well was 30 µL. The enzymatic reaction was run at room temperature for 3 h (2 h for PERK) and then terminated by spotting 4.5 µL of the reaction mixture onto a phosphocellulose membrane. Membranes were washed with 0.5% phosphoric acid (3X ten min each wash), dried and the radioactivity was determined by phosphorimaging with a GE Typhoon FLA9000 scanner. The scanned membranes were quantified using ImageQuant and converted to percent inhibition. Data was analyzed using Prism Graphpad software and the IC50 values were determined using non-linear regression analysis.

In vitro RNase assay: 5'-Carboxyfluorescein (FAM) –and 3'-Black Hole Quencher (BHQ)-labeled XBP1 single stem-loop mini-substrate (5'FAM-CUGAGUCCGCAGCACUCAG-3'BHQ) was purchased from Dharmacon. 0.2 µM IRE1α* was incubated with inhibitors or DMSO for 30 min in assay buffer containing 50 mM HEPES, pH=7.5, 1 mM MnCl2, 100 mM NaCl, 2 mM DTT, and 0.01% Brij 97, followed by incubation with 3 µM RNA substrate for 10 min. The reaction was quenched by adding urea to a final concentration of 4M, and the fluorescence was detected on a Wallac 1420 Victor multifunction plate reader with excitation and emission wavelengths of 485 nm and 535 nm, respectively. The fluorescence intensities were normalized by setting the signal for the reaction with IRE1α* and DMSO to 1 and the reaction without IRE1α* to 0.

Phosphomapping sample preparation: A solution containing 3 uM untreated or dephosphorylated IRE1α 469/547, 0.02% sodium deoxycholate and 10% trichloroacetic acid was

kept on ice for 10 min. The protein precipitate was separated out by centrifugation. The supernatant was discarded. The pellet was washed once with cold acetone, and allowed to air dry. The pellet was resuspended in a 60:1 mixture of 8M urea and 144 mM iodoacetamide. The solution was incubated for 30 min in the dark following which it was added to a mixture containing 5 uM CaCl2 and 1 uL of 1 mg/mL tryspin in 200 mM Tris pH 8.0. The solution was homogenized immediately and incubated at room temperature overnight. 1-2 uL of each sample was injected for MS analysis. Tryptic peptides were identified using SEQUEST. Identity of the peptides of interest was confirmed by matching their fragment spectrums.

References

1 van Anken, E. & Braakman, I. *Crit. Rev. Biochem. Mol. Biol*., **40**, 269-83 (2005).

2 Travers, K. J. et al. *Cell*, **101**, 249-58 (2000).

3 Zhang, K. & Kaufman, R. J., *Cell*, **124**, 587-599 (2006).

4 Brodsky, J. L. & McCracken, A.A., *Semin Cell Dev Biol.*, **10**, 507-13 (1999).

5 Meusser, B. et al., *Nat Cell Biol.*, **7**, 766-72 (2005).

6 Walter, P. and Ron, D., *Nat Rev Mol Cell Biol*., **8**, 519-29 (2007).

7 Merksamer, P. I. & Papa, F. R. J. *Cell. Sci.* **123**, 1003-1006 (2010).

8 Papa, F., *Cold Spring Harb Perspect Med*., **2** (2012).

9 Shore, G. C., Papa, F. R., Oakes, S. A., *Curr Opin Cell Biol*., **23**, 143-9 (2011).

10 Credle, J. J., Finer-Moore, J. S., Papa, F. R., Stroud, R. M. & Walter, P. *Proc. Natl. Acad. Sci. USA* **102**, 18773-18784 (2005).

11 Zhou, J. et al. *Proc. Natl. Acad. Sci. USA* **103**, 14343-14348 (2006).

12 Calfon, M. et al. *Nature* **415**, 92-96 (2002).

13 Yoshida, H., Matsui, T., Yamamoto, A., Okada, T. & Mori, K. *Cell* **107**, 881-891 (2001).

14 Lee, A. H., Iwakoshi, N. N., Glimcher, L. H., *Mol Cell Biol*, **23**, 7448–7459 (2003).

15 Han, D. et al. *Cell* **138**, 562-575, (2009).

16 Hollien, J. et al., *J. Chem Biol*, **186**, 323-331 (2009).

17 Upton, J. P., Wang, L., Han D., Wang, E. S., Huskey, N. E., Lim, L., Truitt, M., McManus, M. T., Ruggero, D., Goga, A., Papa, F. R., Oakes, S. A., *Science*, **338**, 818-22 (2012).

18 Tirasophon, W., Welihinda, A. A. & Kaufman, R. J. *Genes Dev.* **12**, 1812-1824 (1998).

19 Papa, F. R., Zhang, C., Shokat, K. & Walter, P. *Science* **302**, 1533-1537 (2003).

20 Korennykh, A. V. et al. Nature 457, 687-693 (2009).

21 Liu, Y. & Gray, N. S. *Nat. Chem. Biol.* **2**, 358-364 (2006).

22 Ranjitkar, P., Brock, A. M. & Maly, D. J. *Chem. Biol.* **17**, 195-206 (2010).

23 Wang, L., Perera, B. Gayani K., Hari, S. B., Bhattarai, B., Backes, B. J., Seeliger, M. A., Schurer, S. C., Oakes, S. A., Papa, F. R. & Maly, D. J. *Nat. Chem. Biol.* **8**, 982-989 (2012).

24 Ron, D.; Walter, P. *Nat. Rev. Mol. Cell Biol*.,**8**,519−529 (2007).

25 Blais, J. D.; Addison, C. L.; Edge, R.; Falls, T.; Zhao, H.; Wary, K.; Koumenis, C.; Harding, H. P.; Ron, D.; Holcik, M.; Bell, J. C. *Mol. Cell. Biol*., **26**, 9517−9532 (2006).

26 Shi, Y.; Vattem, K. M.; Sood, R.; An, J.; Liang, J.; Stramm, L.;Wek, R. C. *Mol. Cell. Biol*., **18**, 7499−7509 (1998).

27 Marciniak, S. J.; Garcia-Bonilla, L.; Hu, J.; Harding, H. P.; Ron,D. *J. Cell Biol*., **172**, 201−209 (2006).

28 Zhou D, Palam LR, Jiang L, Narasimhan J. et al. J Biol Chem., **283**, 7064–7073 (2008).

29 Akinc, A. et al. *Nat Biotechnol* **26**, 561-569 (2008).